Mechanism of Stoichiometrically Governed Titanium Oxide Brownian Tree Formation on Stepped Au(111)

Robert H. Lavroff,[1] Jason Wang,[2] Michael G. White,[2,3] Philippe Sautet,[1,4,5,*] and Anastassia N. Alexandrova[1,5*]

[1]Department of Chemistry and Biochemistry, [2]Department of Chemistry, Stony Brook University, Stony Brook, New York 11794, USA, [3]Chemistry Division, Brookhaven National Laboratory, Upton, New York 11973, USA [4]Department of Chemical and Biomolecular Engineering, and [5]California NanoSystems Institute, University of California, Los Angeles, Los Angeles, CA 90095-1569, USA

[*]Corresponding authors' emails: sautet@ucla.edu, ana@chem.ucla.edu

Abstract: Previously observed formation of sub-stoichiometric titanium oxide dendritic structures across terraces of Au(111) are computationally studied and shown to follow the classical fractal formation mechanism of diffusion limited aggregation (DLA). Globally optimized gas-phase oxide cluster structures were sampled in a variety of landing formations on gold surfaces and shown to favor isomers driving polymerization to Brownian tree fractal structures. Mobility of Ti_3O_5 monomers is shown to be extremely high, with diffusion barriers of 0.21 eV or less. Through bonding stabilization, polymerization of these monomers is energetically favorable and irreversible on the 111 terrace, but geometrically impossible to propagate along the step edge. Simulated STM images show strong similarity to experiment. By contrast, observation of Ti_3O_6 aggregating as wires along step edges is explained by affinity of oxygen to step edges and statistical arguments for aggregation entropy at the step, in addition to low barriers for monomer diffusion and polymerization.

TOC Graphic:

n·Ti₃O₅(g) + Au(111) → (Ti₃O₅)ₙ Brownian Trees
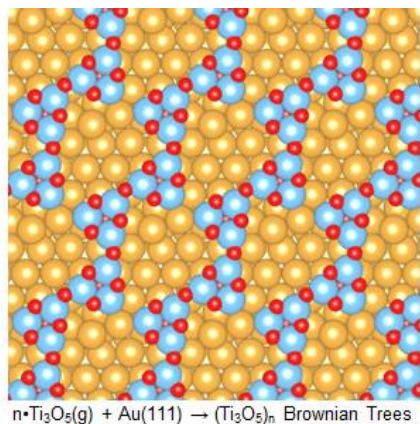
Introduction

Inverse catalysts consisting of metal oxide nanostructures supported on a metallic support are of interest in heterogeneous catalysis as models to probe interfacial electronic structure and reactivity and for the properties of the supported nano-oxide, which often differ from the bulk.[1–3] In some cases, the inverse configuration can enhance catalytic activity[4,5] and is representative of the active phase in industrial oxide supported catalysts.[6] In this work, we focus on the TiO_x/Au(111) inverse catalysts that have been shown to be more active for low-temperature CO-oxidation than their conventional metal-on-oxide counterparts.[7] Using mass-selected cluster deposition, Goodman et. al. observed[8] that when the stoichiometric Ti_3O_6 clusters were soft-landed on a Au(111) surface, they would mostly bind to the step edge, as expected due to oxygen's affinity for under-coordinated gold (reproduced in Figure 1a).[9] In depositing the sub-stoichiometric Ti_3O_5 clusters, however, the observed formation of dendritic structures, developing on surface terraces and nucleating from the step edge (Figure 1b). The assembly size distributions for the as-deposited Ti_3O_5/Au(111) and Ti_3O_6/Au(111) surfaces at room temperature (RT) are shown in Figure S1 (Supporting Information). Furthermore, unlike metal-metal dendritic structures previously observed[10], they did not shift to more compact 2D islands when annealed past 500 K. The stoichiometry, morphology and evolution of inverse catalytic systems at catalytically relevant temperatures are of interest, since these affect the nature and number of available active sites. Hence, density functional theory (DFT) calculations were performed to elucidate the mechanisms of fractal formation, and the differences apparently brought forth by the oxide cluster stoichiometry.

We study the structures of the Ti_3O_x monomers on gold, the barriers to their diffusion, and the mechanism for their dimerization/polymerization. In particular, high mobility of the Ti_3O_5 monomers on the terrace, and strongly favorable dimerization accompanied by surface deformation are shown to lead to fractal-like structures. In addition, we report the energetic and statistical effects leading to the formation of dendritic oxide structures spanning the terraces of stepped Au(111). The found structures are confirmed via simulated scanning tunneling microscopy (STM) images compared to experimental *in situ* STM. We show that the main mechanism of fractal formation to fall in the category of diffusion limited aggregation (DLA), a phenomenon during which particles undergoing Brownian motion experience clustering. These clusters are referred to as Brownian trees and take a fractal-like form.[11] The DLA mechanism for the formation of fractal-like structures on surfaces requires high mobility of the particles during deposition and irreversible binding following particle encounters, i.e., a "hit-and-stick" model.[10,12–15] Here DLA is driving morphological changes of catalytically relevant interfaces, but similar structures have been reported for a wide range of supported clusters including AlF_3 on Cu,[16,17] LiF on Ag,[18,19] MoS_2 on $SrTiO_3(001)$,[20] CeO_2 on graphene/Ru(0001),[21] C_{60} on graphite,[22] and Cu^{23} and W^{24} clusters on graphite.
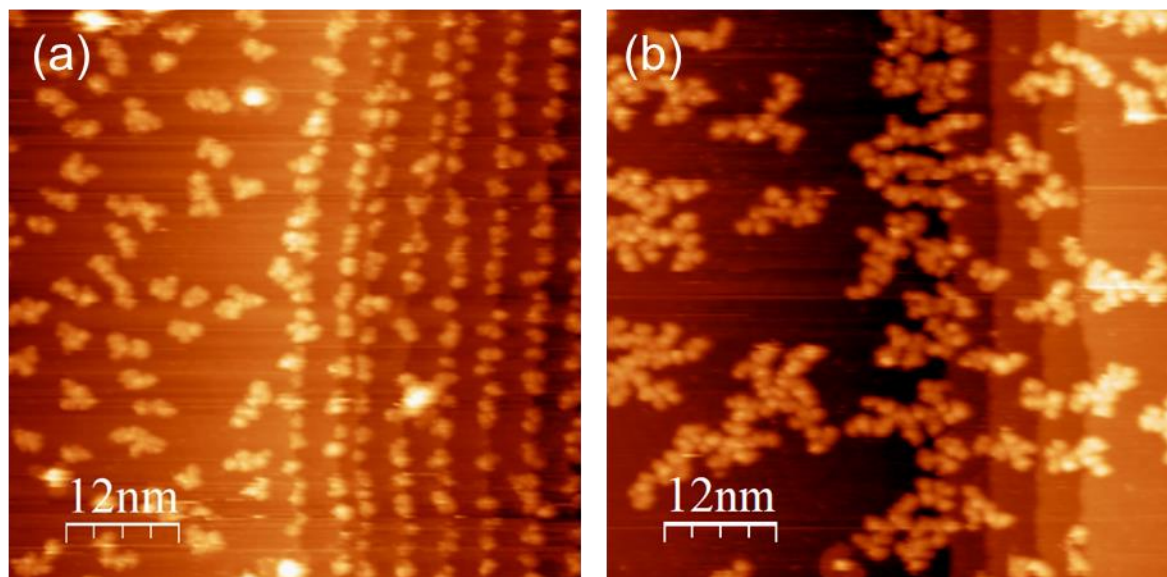

Figure 1: STM images of the as-deposited surfaces for (a) Ti_3O_6 and (b) Ti_3O_5 clusters on Au(111) taken at room temperature. The cluster coverage is 0.25ML for both surfaces. Scan conditions: (a) U=2.0V, I=300pA and (b) U=2.0V, I=200pA. Image sizes are 60 nm×60 nm. For more details, see reference [8].

Computational methods

We first performed global optimizations of Ti_3O_5 and Ti_3O_6 in the gas phase, within a cubic unit cell of length 18 Å along each lattice vector, using our in-house Parallel Global Optimization of gas phase and surface systems (PGOPT) code, which leverages a bond length dissociation algorithm (BLDA) to stochastically sample structures and locate minima.[25,26] The global minima (GM) for each were found to be singular most stable (and thus, thermodynamically predominant) configurations, and so they were used as seeds to sample the structures of supported clusters. They were landed on Au(111) and Au(553) surfaces (the 553 Miller index corresponds to a 111 terrace with a 111 step) in all possible geometric configurations and relaxed (see Note S1 on details of the sampling procedure), then Boltzmann ensembles of isomers[27] were established at a variety of annealing temperatures. This approach circumvents the computationally intractable direct sampling of oxide clusters on the gold slab. From the identified monomer configurations, possible routes of traversing the surface and dimerization were determined, and the dimerization energies and barriers were computed. All calculations were performed with periodic DFT, using the Vienna Ab-Initio Software Package (VASP),[28–30] in the projector-augmented wave (PAW) basis set with an energy cutoff of 400 eV. The Perdew–Burke-Ernzerhof (PBE) functional was used with corresponding pseudopotentials, and a rotationally invariant Hubbard U[31] correction of 2.5 eV was applied to the d-orbitals of titanium. Prior literature reports U-values of 2.5 to 4.5 eV as acceptable values, and as benchmarking showed little difference in energetics between these two values, the lower bound was selected to help convergence.[32,33] The zero damping DFT-D3 method of Grimme[34] was used to account for van der Waals corrections, and initially a dipole correction in the Z-direction was applied; however, benchmarking against otherwise identical calculations without this dipole correction showed it could be removed without change in energetics, speeding up convergence for large unit cells. To avoid unwanted interaction between titania clusters, a 6x6 Au supercell was used with 6 layers for the Au(111) surface, and a 1x6 (i.e. one terrace that is six atoms wide) supercell with 6 layers for the Au(553) surface. The top two of these layers were unconstrained during optimization to allow for any surface deformation. A 12 Å vacuum was used to avoid interaction between slabs. A 1x1x1 gamma K-point scheme was applied, justified by the large size of the supercell (the 111 surface is approximately 324 square Å in area, while the 553 surface has an approximate area of 216 square Å). Second order Methfessel-Paxton smearing was

used to assist convergence, but all energies were taken in the limit of zero smearing. Climbing image nudged elastic band (CINEB) calculations and Bader charges were computed using the VASP plugins of Henkelman et. al.[35–40] Sampling of gas phase structures on Au surfaces were done with the Atomic Simulation Environment (ASE) graphical user interface.[41,42] Visualization of Bader charges were done in Jmol.[43–45] All other visualization was done with Vesta.[46–49]

Results and Discussion

1. Ti_3O_5

Monomers. The GM of Ti_3O_5 in gas phase is highly dominant at experimental annealing temperature (700 K). The five most stable isomers are shown in Figure S2, and the same are shown for Ti_3O_6 in Figure S3 in the SI. Previous literature showing gas phase isomer ensembles of transition metal oxides are generally smaller than those of metal clusters support that our sampling is comprehensive.[50–53] One oxygen atom in the GM cluster is coordinated to a single Ti atom, rather than bridges between two Ti atoms, forming a Ti-oxo motif. This atom protrudes upward from the cluster, as a sort of "handle". This handle atom, while negatively charged, is slightly electron deficient compared to the other oxygens in the supported cluster, as shown by the Bader charges in Figure 2a. This gas phase GM cluster is predicted by DFT+U to be an open shell singlet with two unpaired electrons in the d_z^2 orbitals of the two "handle-free" Ti atoms. This is demonstrated clearly by its calculated spin density, shown in Figure S4. It should be noted that the spin-polarized unrestricted Kohn-Sham (UKS) DFT formalism used here, where separate density matrices/Slater determinants are obtained for spin-up and spin-down electrons, breaks spin symmetry and allows for the presence of an open shell singlet, a state normally only computable by multiconfigurational methods.

Upon placement on Au(111) and sampling, the identified surface-supported GM, with a binding energy of -4.06 eV, remains fairly close in structure to its gas phase analogue (Figure 2b), and is also a highly-predominant configuration (Figure 3). The second lowest-energy isomer (LM1) is 1.01 eV above GM. This structure can be seen as the GM lying completely flat on the Au(111) surface (Figure 2c). The structure largely retains the geometric and electronic features of GM, including the "handle" O atom with a slightly reduced negative charge. While LM1 is

thermodynamically inaccessible as a monomer (Figure 3), it will become key in the polymerization process described below. One isomer dominates the population of on the 553 step edge as well, which strongly resembles the geometry of the terrace GM and adopts similar Bader charges (Figure 2d and Figure 4). Ti_3O_5 binds strongly at the bottom of the step with a binding energy of -8.89 eV, interacting both with the terrace (Ti-Au bond lengths of 2.66 and 3.07 Å) and the step edge (O-Au bond length of 2.64 and Ti atoms sitting in the interstitial sites of Au at distances from 2.66 to 3.07 Å). The flat-lying isomer is stabilized by the step (LM3) and is 0.65 eV less stable than the more vertical GM, compared to 1.01 eV for the (111) surface.
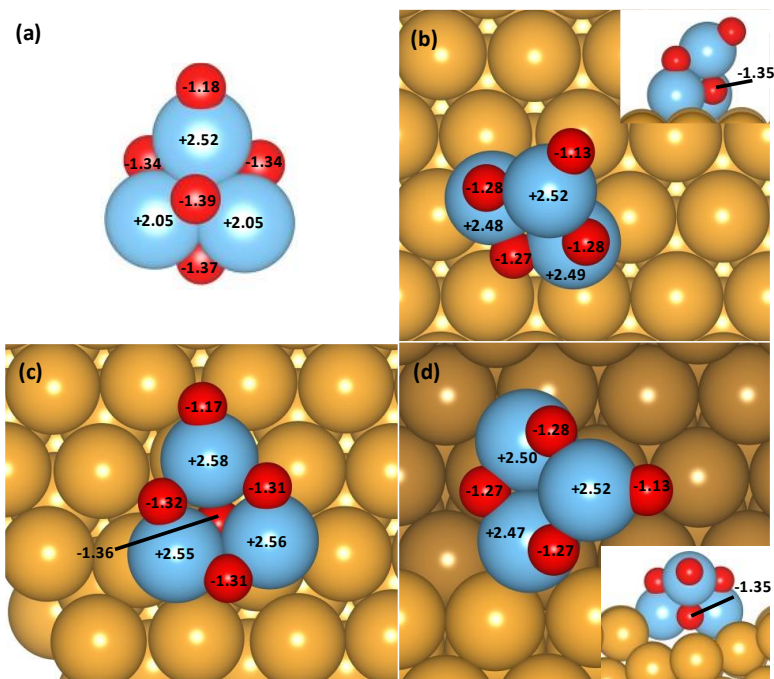

Figure 2: a) Gas phase GM of Ti_3O_5 b) GM of Ti_3O_5 on the terrace, where the "handle" oxygen is far from the surface. c) Key isomer (LM1) of Ti_3O_5 to build fractal-like polymers on the terrace or propagating from the step. d) Global minimum of Ti_3O_5 on the step, which is nearly identical to the GM on the terrace.
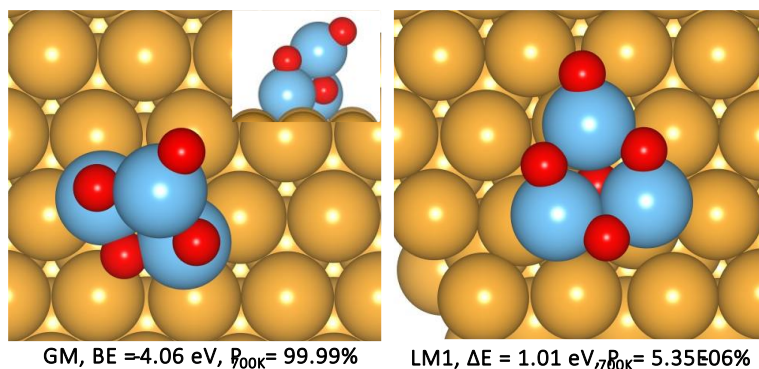
Figure 3: Structures of Ti$_3$O$_5$ isomers at the Au(111) terrace, and their Boltzmann population (P$_{700K}$) at maximum annealing temperature (700K). Energy difference is relative to GM.
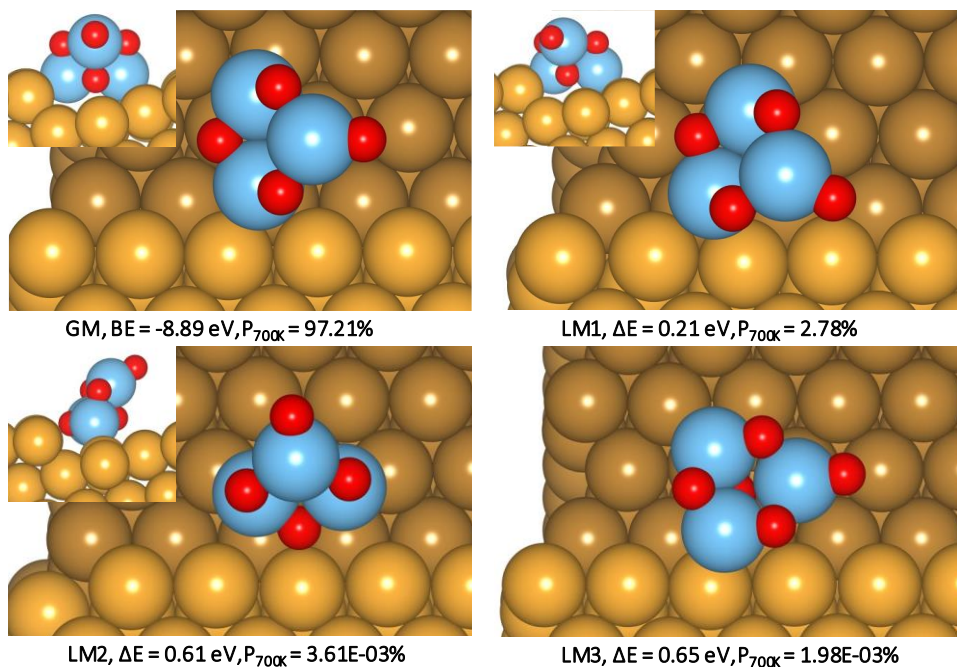

Figure 4: Structures of Ti$_3$O$_5$ isomers at the step edge, and their Boltzmann population (P$_{700K}$) at maximum annealing temperature (700K). Energy differences are relative to GM.

Monomer migration on the surface. The mobility of monomers on the surface, i.e. their barrier to translation, should be key to the mechanism of fractal formation. Climbing-image nudged elastic band (CINEB) calculations were performed for the diffusion of the Ti$_3$O$_5$ GM on Au(111).

The barrier to translate directly over an Au atom along the lattice vector (the steepest possible translation trajectory) is very low, 0.21 eV (Figure 5a). Though LM1 of Ti_3O_5 comprises an insignificant portion of the statistical ensemble, this isomer also diffuses easily on the surface, with a translational barrier of 0.16 eV (Figure 5b). We conclude that overall cluster mobility on the surface is very high, presenting no hindrance for cluster aggregation to form fractals.
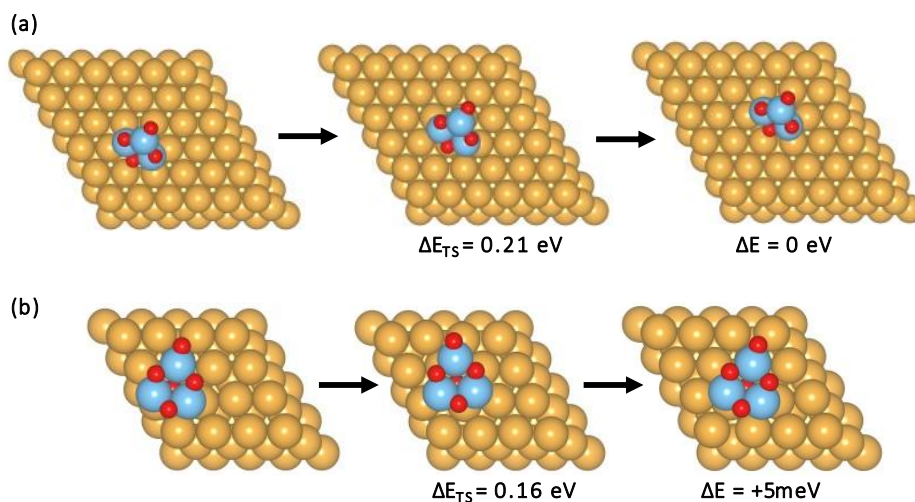
(a)

$\Delta E_{TS} = 0.21$ eV $\Delta E = 0$ eV

(b)

$\Delta E_{TS} = 0.16$ eV $\Delta E = +5meV$

Figure 5: Diffusion barriers for the Ti_3O_5 a) GM monomer and b) LM1 monomer. The full CINEB pathways for both monomer translations can be found in Figures S5 and S6 in the SI.

Cluster dimerization. Given the facile monomer migration on the surface, the next step in the possible fractal formation is dimerization. The upright GM does not appear suitable for polymerization. However, the dimer resulting from the bonding of GM via the electron deficient "handle" O to Ti in another Ti_3O_5 GM is found to be a highly stable configuration that lies flat, mimicking that of the monomer LM1 (Figure 6). The dimerization energy is -2.197 eV, i.e. greater in absolute value than the sum of the two penalties for isomerization from GM to LM1, based on thermodynamics. Note that the "handle" oxygen atom on the end of the dimer remains available for the polymer to propagate further. In fact, in the presence of the LM1, GM monomers lay down and polymerize spontaneously (no barrier involved) during DFT geometry optimization, showing a "reverse domino" effect (i.e. monomers fall down in the presence of a nucleation site) which will lead to further polymerization. The system starting from two GMs, while does not dimerize spontaneously, can also dimerize with a small barrier of only 5 meV (compared to the magnitude of thermal fluctuations of $k_BT=25.7$ meV at room temperature and $k_BT=0.06$ eV at 700 K).

Dimerization happens via both GM monomers falling in the same direction on the support and making a bond via the "handle" O atom. The reaction profile is shown in Figure 7 (see also the full pathway in Figure S7). Thus, we can conclude that the process of DLA occurs spontaneously in this system of mass selected Ti_3O_5 clusters on Au(111).

Figure 6: Highly stable dimer predicted to form from Ti_3O_5 monomers - Bader charges.

$\Delta E_{TS} = +5 meV$ $\Delta E = -2.2\ eV$

Figure 7: Barrierless (at finite temperature) and exothermic dimerization of two Ti_3O_5 GM monomers forming a dimer, a Brownian tree nucleation site.

Sampling on the clusters at the step led to more distinct structures (Figure 4), but a single isomer still dominates the Boltzmann population, even at the highest of annealing temperatures. Just as the GM on the 111 terrace, GM on the step edge stands rather upright with a decreased accessibility to the "handle" oxygen for another monomer. This species adopts a nearly identical geometry and Bader charge distribution as the terrace-bound GM (Figure 2d). LM1 at the step edge is also an analogue of LM1 on the terrace (this time 0.65 eV higher in energy than GM). The structure of LM1 appears predisposed to propagate the fractals from the step edge, since the cost to form the flat isomer is reduced.

On the other hand, we find upon sampling all possible geometries that the Ti_3O_5 dimer GM formed at the step has no way of propagating further along the step, as the "handle" oxygen atom is pointing far from the step and inaccessible to the next monomer (Figure 8). In calculation setups, purposely pointing this handle toward the step for further polymerization proved futile, as geometry optimization relaxed the structure back to pointing away. The only way Ti_3O_5 on the step could continue to polymerize is by moving away from the step edge, supporting experimental STM images where some Brownian trees nucleate at the step and grow in the direction orthogonal to it.
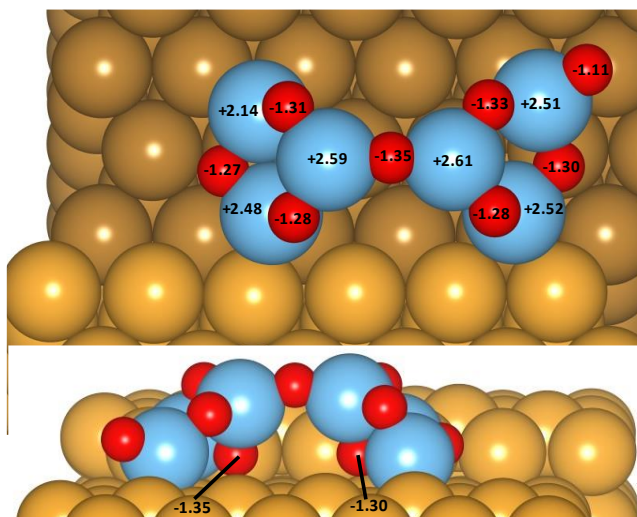
Figure 8: Top and side view of the Ti_3O_5 dimer GM at the step. This structure is stable, with a binding energy of -3.58 eV, but cannot result in a polymer along the step edge due to the "handle" oxygen (Bader charge = -1.11 |e|) pointing away from the step.

Analysis of energetics pertaining to the irreversible dendritic wire formation. Monomers of Ti_3O_5 on the terrace assume a charge of +1.22 |e| (in LM1) or +1.19 |e| (in GM), indicating strong cluster-support interaction (as also indicated by the large adsorption energy). It is rather surprising that, given that strong interaction, the monomers remain mobile on the surface (*vide supra*). An additional factor contributing to the mobility comes from the response of the support to the cluster binding. We find that the top monolayer of the Au(111) surface undergoes substantial deformation upon cluster and polymer binding (see Figure 9). We calculated the deformation penalty on the 111 surface for a Brownian tree polymer and compared it to GM and LM1 monomers, as well as the dimer in Figure 6. For that, first, due to the fact that surface calculations require periodic

boundary conditions (PBC) and fractals do not have traditional translational symmetry, we created a "dendritic wire" model which spans the PBC at a similar atom density as the Brownian trees shown in experiment (shown as a single unit cell and a supercell in Figure 9). The need for a 4x4 unit surface, allowing the dendritic wires to span many unit cells, does introduce artificial Ti-Ti interactions, circled in red in Figure 9a. These are not expected to affect surface deformation analysis in any appreciable way, since in a true Brownian tree, an oxygen atom would bridge these two Ti atoms far above the Au surface.
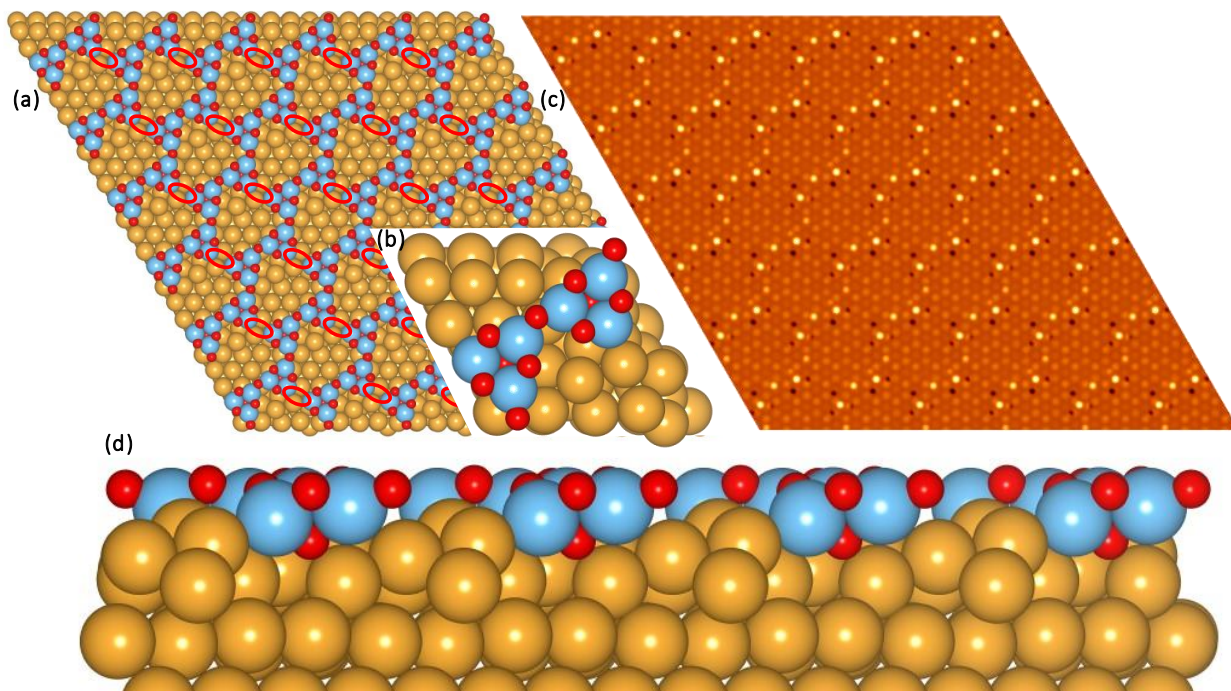
Figure 9: Dendritic wire model shown as a) a 12x12 supercell, b) a 4x4 unit cell, c) a simulated STM image of the dendritic wire model. The lattice vector length of this supercell is approximately 4 nm. d) A side view of the supercell demonstrating the drastic surface deformation

We employ a surface binding flavor of the distortion/interaction models of Morokuma[54,55], Bickelhaupt[56–58], and Houk[58–60] in which the dendritic wire is separated from the deformed gold surface and each is optimized separately. Compared to its single point energy, the distorted Au(111) surface gains 2.1 eV in stability for a 4x4 unit cell when re-optimized back to its original (111) geometry. This 2.1 eV is the energetic penalty that the surface pays for deformation. This costly deformation indicates that the surface would want to get rid of the polymer, especially compared to the penalty of the GM monomer (0.36 eV) and LM1 monomer's (0.98 eV) surfaces.

This 2.1 eV penalty is, however, overcompensated by significant polymerization energy, plus the energy of binding the clusters to the surface. We compute a dimer stabilization, i.e. the binding energy of the dendritic wire (with two gas phase monomers and a pristine Au surface as reference) minus twice the binding energy of the GM monomer, normalized by a factor of 1/2 due to two dimer bonds per unit cell, to be 4.62 eV. We conclude that the surface deformation caused by Brownian tree formation is overcompensated quite substantially, by 2.52 eV. Likewise, for the dimer in Figure 6, we compute a deformation penalty of 1.67 eV overcompensated by 2.52 eV of dimer stabilization (0.85 eV overall energy compensation), calculated in the same way as the dendritic wire but excluding the prior factor of 1/2 since we now have only one dimer bond per unit cell. Hence, the experimentally observed irreversible Brownian tree formation is attributed to the significant energetic gain from polymerization, despite the surface deformation penalty. The analysis further suggests that the larger the Brownian tree grows, the more irreversible it becomes.

Simulated STM. For further support of experiment, we use computed partial charge densities to simulate a scanning tunneling microscopy (STM) image of these dendritic wires. The image in Figure 9c was computed at constant height mode 9 Å from the topmost atom in the unit cell with a positive sample bias of 0.8 eV (i.e. sampling bands from the Fermi level down to 0.8 eV below the Fermi level). Experimental results use a positive sample bias of approximately 2 eV at constant current mode[8], but extensive benchmarking of heights and biases showed that adjustments needed to be made for a simulated STM to obtain the clearest possible image.

2. Ti_3O_6

Monomers. Upon sampling in all possible configurations on the 111 and 553 surfaces, three isomers on Au(111), and two on Au(553) were found to dominate the corresponding Boltzmann populations at 700 K (Figures 10 and 11). The GMs for Au(111) and Au(553) with computed atomic Bader charges are shown in Figure 12. All terrace minima show a mix of Ti-Au and O-Au bonds for surface binding, while step minima show a strong (known[9]) preference for binding via oxygen. The surface-cluster charge transfer is minimal for this cluster stoichiometry, with the cluster adopting a total positive charge of +0.04 |e| on Au(111) and +0.14 |e| on Au(553). This is expected since Ti in the Ti_3O_6 cluster is d^0, and hence the cluster establishes only dative interactions with the Au surface.

GM, BE =-3.31 eV,
P_{700K}= 99.95%

LM1, ΔE = 0.44 eV,
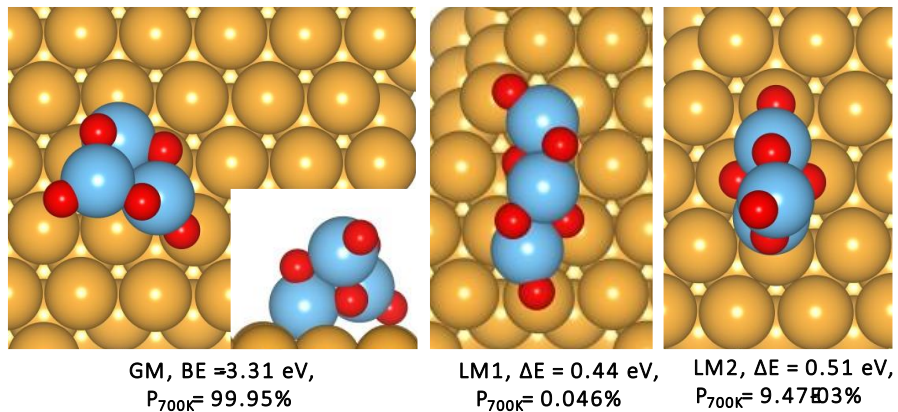P_{700K}= 0.046%

LM2, ΔE = 0.51 eV,
P_{700K}= 9.47E03%

Figure 10: Structures of Ti_3O_6 isomers at the Au(111) terrace, and their Boltzmann population (P_{700K}) at maximum annealing temperature (700K). Energy differences are relative to GM.

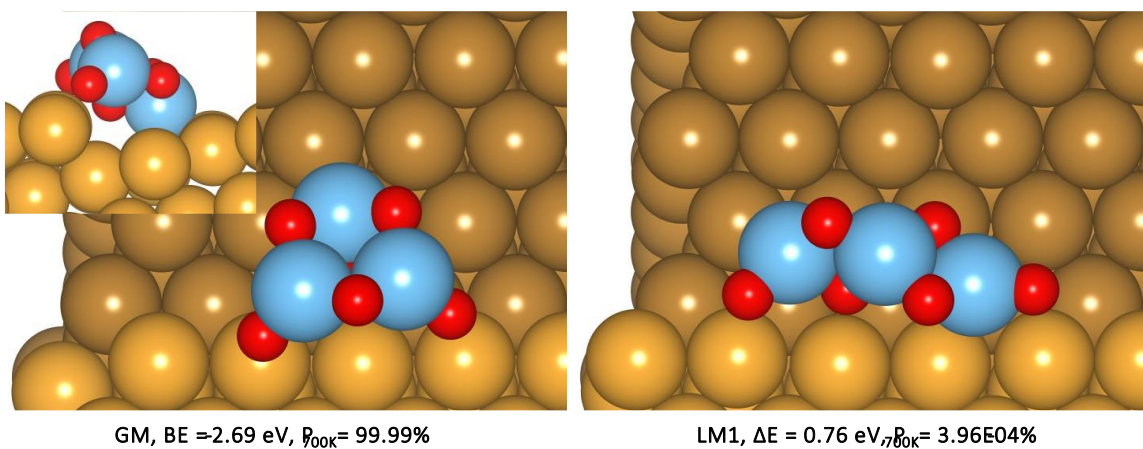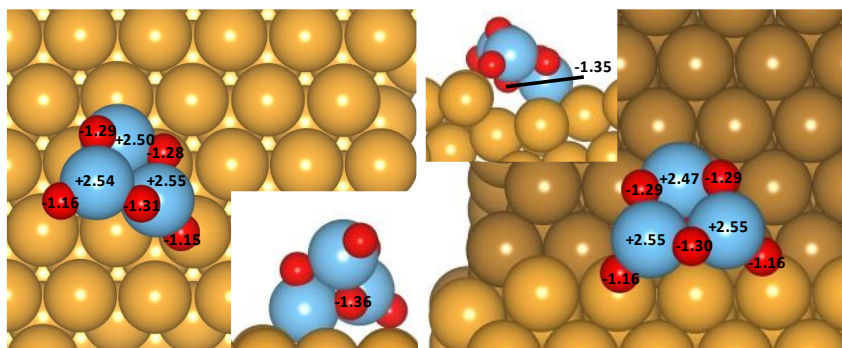GM, BE =-2.69 eV, P_{700K}= 99.99%

LM1, ΔE = 0.76 eV, P_{700K}= 3.96E04%

Figure 11: Structures of Ti_3O_6 isomers at the step edge, and their Boltzmann population (P_{700K}) at maximum annealing temperature (700K). Energy difference is relative to GM.

13

Figure 12: Global minima of Ti$_3$O$_6$ on Au(111) (left) and Au(553) (right), with Bader charges on atoms indicated. Ti: blue, O: red.

Cluster dimerization and fractal formation along the step edges. For Ti$_3$O$_6$, small cluster aggregates form on the terrace in experiment, and fibrils (with length depending on coverage) form along the step edge. The monomer is computed to be more stable on the terrace than on the step edge, however. The binding energy of GM on Au(111) is -3.31 eV, and on Au(553) it is -2.69 eV, i.e. 0.62 eV less stable. The unexpected preference for the step seen in experiment is readily explained by ease of monomer diffusion across the terrace and electrostatic attraction between these monomers and undercoordinated Au atoms at the step. CINEB calculations show a low diffusion barrier of 0.10 eV for the Ti$_3$O$_6$ GM along the terrace (Figure 13, full trajectory in Figure S8). Furthermore, QTAIM analysis[61–63] shows that when the terrace GM geometry is placed near the step (closest Ti-step distance of 5.15 Å, closest O-step distance of 3.6 Å), prominent non-covalent interactions occur as shown in Figure S9. Even more notably, this structure merely relaxes to the step GM when a geometry optimization is performed.
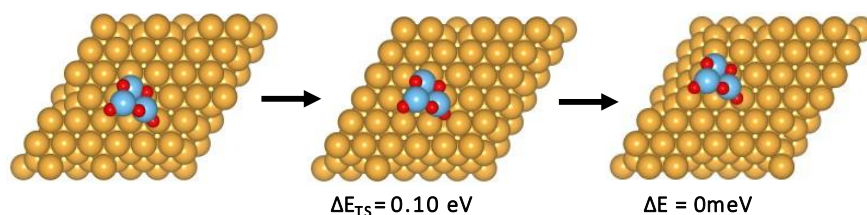
Figure 13: Diffusion of Ti$_3$O$_6$ monomer along the lattice vector of the Au(111) terrace.

Two possible mechanisms of Ti$_3$O$_6$ dimerization on the step exist: one involves the monomer GM dimerizing to form a dimer LM, and one involves the monomer LM1 dimerizing to form a dimer GM. CINEB calculations show diffusion barriers of 0.26 eV for the Ti$_3$O$_6$ GM (Figure 14a, S10)

and 0.38 eV for the LM1 (Figure 14b, S11) along the step. We clarify here that the dimer comprised of two LM1 monomers is the lower in energy and thus referred to as the GM dimer, whereas the dimer of two GM monomers is higher in energy and thus referred to as the LM dimer.
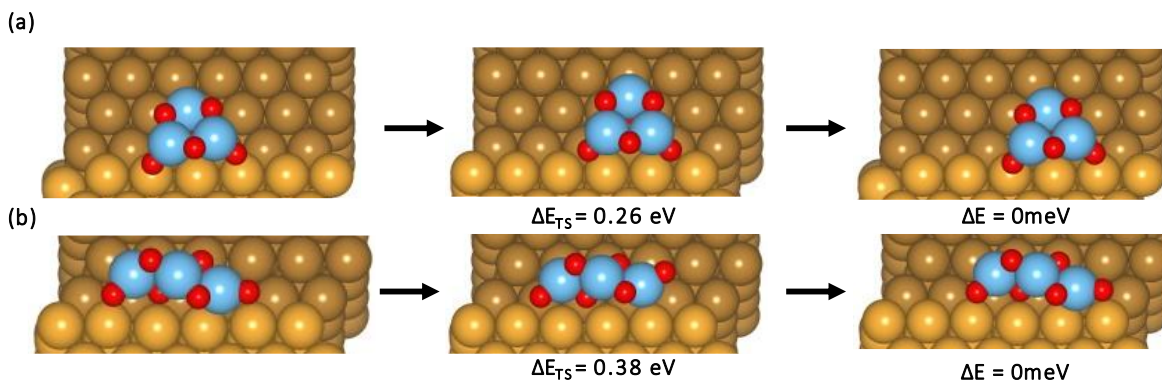

Figure 14: Diffusion barrier of Ti_3O_6 at the Au step (a) GM and (b) LM1 across the step edge. These low barriers make cluster di/polymerization highly accessible despite the strong binding of monomers to the step.

In the LM dimer, the GM monomers pack with approximate inversion symmetry to each other, allowing this unit to continue propagating *ad infinitum*, or until coverage limits it. Furthermore, its electron deficient "handle" oxygen atoms will readily form bonds with the nearby monomer on the step (Figure 15a). Four Ti-O bonds are being formed and dimerization at the step is exothermic, with a computed binding energy of -7.24 eV and dimerization energy of 1.86 eV. However, relaxation of an inverted GM monomer resulted in a LM that is 1.72 eV higher in energy than GM, making the dimerization process only weakly favorable by 0.04 eV. Alternatively, the GM dimer (Figure 15b) is a near-perfect wire with a binding energy of -8.04 eV and dimer energy of -4.18 eV. The process by which the monomer GM would isomerize to a LM1 is not clear and thus a set of barriers was not computed, but thermodynamically this costs 0.76 eV to occur per monomer or 1.72 eV per dimer formation, hypothesized accessible by multiple intermediate steps for an overall stabilization of -2.46 eV. Thus, we hypothesize the polymerized fibrils to take the geometry of the GM dimer in Figure 15b.
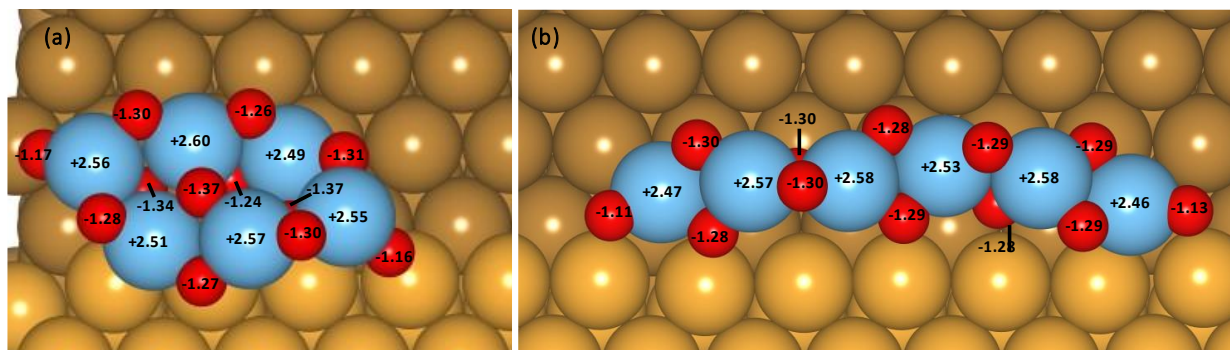
15

Figure 15: Dimers of the Ti_3O_6 (a) GM and (b) LM1 monomers, which pack symmetrically and can continue to polymerize using electron-deficient "handle" oxygen atoms.

Despite the electrostatic attraction of the terrace GM cluster to the step, the step GM is 0.62 eV less stable than the terrace GM. Thus, stochastic monomer migration both toward and away from the step takes place. In this context, we attribute fibril formation to an additional factor of entropy as follows: during diffusion, entropy would favor clusters "parking" at the step-edge because the clusters can diffuse away only in the direction orthogonal to the step. This statistically creates lines of clusters faster than the monomers have a chance to diffuse away (though the kinetics of all involved steps is not computed in this work, due to computational expense). Once clusters polymerize along the step edge, they are stabilized sufficiently to stay. This is in contrast to Ti_3O_5, which is unable to form a polymer along the step edge.

Some Ti_3O_6 polymers do form on the terraces. This is suspected to take place via the same dimerization process as the freely diffusing GM monomers on the step (i.e. similar to Figure 15a geometry), but at lower frequency due to competition with the monomers being entropically drawn to the step instead. Taken together, these arguments lead us to the hypothesized origin of polymer formation preferentially at the step for Ti_3O_6.

Conclusions

Using global optimization and DFT calculations, we conclude that Goodman et al.'s hypothesis[8] of diffusion limited aggregation as the mechanism for fractal-like structures of Ti_3O_5 on stepped Au(111) is correct, and provide atomistic detail for the process. We show that DLA is driven by energetically and kinetically favored "key" dimer geometries serving as nucleation sites. Importantly, extremely high monomer mobility allow diffusion to serve as the primary mode of transport along the surface. The dimerization is barrierless and the energetic gain from it is

significant, despite the surface deformation penalty and the need for the cluster to isomerize to the higher-energy LM1, making the dimer formation irreversible. The increase in deformation penalty overcompensation by cluster-cluster binding is even more significant as more monomers are added to the chain, as shown in our periodic "dendritic wire" model. Thus, the stability of the Brownian trees and their dimer nucleation sites, even at high annealing temperatures, is attributed exclusively to the strong Ti-O bonds that form between the clusters during polymerization. The aggregation of Ti_3O_6 along the step edge is explained by statistical entropy and bonding energetics, whereas this phenomenon is ruled out for Ti_3O_5 by its inability to form a polymer along the step. The results in this study uncover first-principles information about surface transport phenomena on an effective "inverse" catalyst and present a generalizable approach to *ab initio* mechanism elucidation for other observed fractal structures in this class of catalytic systems.[64]

Supporting Information

Supplemental images, discussion of sampling strategy and BLDA algorithm, formulae for binding and dimerization energies, discussion of DFT accuracy benchmarking, discussion of STM simulations.

Acknowledgements

References

(1) Schoiswohl, J.; Sock, M.; Chen, Q.; Thornton, G.; Kresse, G.; Ramsey, M. G.; Surnev, S.; Netzer, F. P. Metal Supported Oxide Nanostructures: Model Systems for Advanced Catalysis. *Top. Catal.* **2007**, *46* (1–2). https://doi.org/10.1007/s11244-007-0324-6.

(2) Rodríguez, J. A.; Hrbek, J. Inverse Oxide/Metal Catalysts: A Versatile Approach for Activity Tests and Mechanistic Studies. *Surf. Sci*. 2010. https://doi.org/10.1016/j.susc.2009.11.038.

(3) Rodriguez, J. A.; Liu, P.; Graciani, J.; Senanayake, S. D.; Grinter, D. C.; Stacchiola, D.; Hrbek, J.; Fernández-Sanz, J. Inverse Oxide/Metal Catalysts in Fundamental Studies and Practical Applications: A Perspective of Recent Developments. *J. Phys. Chem. Lett*. 2016. https://doi.org/10.1021/acs.jpclett.6b00499.

(4) Rodriguez, J. A.; Graciani, J.; Evans, J.; Park, J. B.; Yang, F.; Stacchiola, D.; Senanayake, S. D.; Ma, S.; Perez, M.; Liu, P.; Sanz, J. F.; Hrbek, J. Water-Gas Shift Reaction on a Highly Active Inverse CeO, x/Cu(111) Catalyst: Unique Role of Ceria Nanoparticles. *Angew. Chem. – Int. Ed.* **2009**, *48* (43). https://doi.org/10.1002/anie.200903918.

(5) Wu, C.; Lin, L.; Liu, J.; Zhang, J.; Zhang, F.; Zhou, T.; Rui, N.; Yao, S.; Deng, Y.; Yang, F.; Xu, W.; Luo, J.; Zhao, Y.; Yan, B.; Wen, X. D.; Rodriguez, J. A.; Ma, D. Inverse ZrO2/Cu as a Highly Efficient Methanol Synthesis Catalyst from CO2 Hydrogenation. *Nat. Commun.* **2020**, *11* (1). https://doi.org/10.1038/s41467-020-19634-8.

(6) Lunkenbein, T.; Schumann, J.; Behrens, M.; Schlögl, R.; Willinger, M. G. Formation of a ZnO Overlayer in Industrial Cu/ZnO/Al2O3 Catalysts Induced by Strong Metal-Support Interactions. *Angew. Chem. – Int. Ed.* **2015**, *54* (15). https://doi.org/10.1002/anie.201411581.

(7) Palomino, R. M.; Gutiérrez, R. A.; Liu, Z.; Tenney, S.; Grinter, D. C.; Crumlin, E.; Waluyo, I.; Ramírez, P. J.; Rodriguez, J. A.; Senanayake, S. D. Inverse Catalysts for CO Oxidation: Enhanced Oxide-Metal Interactions in MgO/Au(111), CeO2/Au(111), and TiO2/Au(111). *ACS Sus. Chem. Eng.* **2017**, *5* (11). https://doi.org/10.1021/acssuschemeng.7b02744.

(8) Goodman, K. R.; Wang, J.; Ma, Y.; Tong, X.; Stacchiola, D. J.; White, M. G. Morphology and Reactivity of Size-Selected Titanium Oxide Nanoclusters on Au(111). *J. Chem. Phys.* **2020**, *152* (5). https://doi.org/10.1063/1.5134453.

(9) Baker, T. A.; Friend, C. M.; Kaxiras, E. Atomic Oxygen Adsorption on Au(111) Surfaces with Defects. *J. Phys. Chem. C* **2009**, *113* (8). https://doi.org/10.1021/jp806952z.

(10) Hwang, R. Q.; Günther, C.; Schröder, J.; Günther, S.; Kopatzki, E.; Behm, R. J. Nucleation and Growth of Thin Metal Films on Clean and Modified Metal Substrates Studied by Scanning Tunneling Microscopy. *J. Vac. Sci. Technol. A* **1992**, *10* (4). https://doi.org/10.1116/1.578012.

(11) Witten, T. A.; Sander, L. M. Diffusion-Limited Aggregation, a Kinetic Critical Phenomenon. *Phys. Rev. Lett.* **1981**, *47* (19). https://doi.org/10.1103/PhysRevLett.47.1400.

(12) Meakin, P. Formation of Fractal Clusters and Networks by Irreversible Diffusion-Limited Aggregation. *Phys. Rev. Lett.* **1983**, *51* (13). https://doi.org/10.1103/PhysRevLett.51.1119.

(13) Witten, T. A.; Sander, L. M. Diffusion-Limited Aggregation. *Phys. Rev. B.* **1983**, *27* (9), 5686–5697. https://doi.org/10.1103/PhysRevB.27.5686.

(14) Bott, M.; Michely, T.; Comsa, G. The Homoepitaxial Growth of Pt on Pt(111) Studied with STM. *Surf. Sci.* **1992**, *272* (1–3). https://doi.org/10.1016/0039-6028(92)91433-C.

(15) Zhang, Z.; Chen, X.; Lagally, M. G. Bonding-Geometry Dependence of Fractal Growth on Metal Surfaces. *Phys. Rev. Lett.* **1994**, *73* (13). https://doi.org/10.1103/PhysRevLett.73.1829.

(16) Candia, A. E.; Gómez, L.; Vidal, R. A.; Ferrón, J.; Passeggi, M. C. G. An STM and Monte Carlo Study of the AlF3 Thin Film Growth on Cu(1 1 1). *J. Phys. D Appl. Phys.* **2015**, *48* (26). https://doi.org/10.1088/0022-3727/48/26/265305.

(17) Moreno-López, J. C.; Vidal, R. A.; Passeggi, M. C. G.; Ferrón, J. STM Study of the Initial Stages of AlF3 on Cu(100). *Phys. Rev. B* **2010**, *81* (7). https://doi.org/10.1103/PhysRevB.81.075420.

(18) Farías, D.; Braun, K. F.; Fölsch, S.; Meyer, G.; Rieder, K. H. Observation of a Novel Nucleation Mechanism at Step Edges: LiF Molecules on Ag(111). *Surf. Sci.* **2000**, *470* (1–2). https://doi.org/10.1016/S0039-6028(00)00917-1.

(19) Romankov, V.; Dreiser, J. Morphology of Ultrathin Lithium Fluoride Deposited on Ag(100): Dendrites versus Islands. *Phys. Rev. B* **2021**, *104* (19). https://doi.org/10.1103/PhysRevB.104.195401.

(20) Zhang, Y.; Ji, Q.; Wen, J.; Li, J.; Li, C.; Shi, J.; Zhou, X.; Shi, K.; Chen, H.; Li, Y.; Deng, S.; Xu, N.; Liu, Z.; Zhang, Y. Monolayer MoS2 Dendrites on a Symmetry-Disparate SrTiO3 (001) Substrate: Formation Mechanism and Interface Interaction. *Adv. Funct. Mater.* **2016**, *26* (19). https://doi.org/10.1002/adfm.201505571.

(21) Novotny, Z.; Netzer, F. P.; Dohnálek, Z. Ceria Nanoclusters on Graphene/Ru(0001): A New Model Catalyst System. *Surf. Sci.* **2016**, *652*. https://doi.org/10.1016/j.susc.2016.03.020.

(22) Liu, H.; Lin, Z.; Zhigilei, L. V.; Reinke, P. Fractal Structures in Fullerene Layers: Simulation of the Growth Process. *J. Phys. Chem. C* **2008**, *112* (12). https://doi.org/10.1021/jp0775597.

(23) Mondal, S.; Bhattacharyya, S. R. Oxidation Behaviour of Copper Nanofractals Produced by Soft-Landing of Size-Selected Nanoclusters. *RSC Adv.* **2015**, *5* (120). https://doi.org/10.1039/c5ra20694d.

(24) Park, E. J.; Dollinger, A.; Huether, L.; Blankenhorn, M.; Koehler, K.; Seo, H. O.; Kim, Y. D.; Gantefoer, G. The Nano-Fractal Structured Tungsten Oxides Films with High Thermal Stability Prepared by the Deposition of Size-Selected W Clusters. *Appl. Phys. A Mater. Sci. Process.* **2017**, *123* (6). https://doi.org/10.1007/s00339-017-1037-8.

(25) Zhai, H.; Alexandrova, A. N. Local Fluxionality of Surface-Deposited Cluster Catalysts: The Case of Pt7 on Al2O3. *J. Phys. Chem. Lett.* **2018**, *9* (7). https://doi.org/10.1021/acs.jpclett.8b00379.

(26)   Zhai, H.; Alexandrova, A. N. Ensemble-Average Representation of Pt Clusters in Conditions of Catalysis Accessed through GPU Accelerated Deep Neural Network Fitting Global Optimization. *J. Chem. Theory Comput.* **2016**, *12* (12). https://doi.org/10.1021/acs.jctc.6b00994.

(27)   Zhang, Z.; Zandkarimi, B.; Alexandrova, A. N. Ensembles of Metastable States Govern Heterogeneous Catalysis on Dynamic Interfaces. *Acc. Chem. Res.* **2020**, *53* (2). https://doi.org/10.1021/acs.accounts.9b00531.

(28)   Kresse, G.; Furthmüller, J. Efficiency of Ab-Initio Total Energy Calculations for Metals and Semiconductors Using a Plane-Wave Basis Set. *Comput. Mater. Sci.* **1996**, *6* (1). https://doi.org/10.1016/0927-0256(96)00008-0.

(29)   Kresse, G.; Furthmüller, J. Efficient Iterative Schemes for Ab Initio Total-Energy Calculations Using a Plane-Wave Basis Set. *Phys. Rev. B* **1996**, *54* (16). https://doi.org/10.1103/PhysRevB.54.11169.

(30)   Kresse, G.; Hafner, J. Ab Initio Molecular Dynamics for Liquid Metals. *Phys. Rev. B* **1993**, *47* (1). https://doi.org/10.1103/PhysRevB.47.558.

(31)   Dudarev, S.; Botton, G. Electron-Energy-Loss Spectra and the Structural Stability of Nickel Oxide: An LSDA+U Study. *Phys. Rev. B* **1998**, *57* (3). https://doi.org/10.1103/PhysRevB.57.1505.

(32)   Setvin, M.; Franchini, C.; Hao, X.; Schmid, M.; Janotti, A.; Kaltak, M.; van de Walle, C. G.; Kresse, G.; Diebold, U. Direct View at Excess Electrons in TiO2 Rutile and Anatase. *Phys. Rev. Lett* **2014**, *113* (8). https://doi.org/10.1103/PhysRevLett.113.086402.

(33)   Hu, Z.; Metiu, H. Choice of U for DFT+ U Calculations for Titanium Oxides. *J. Phys. Chem. C* **2011**, *115* (13). https://doi.org/10.1021/jp111350u.

(34)   Grimme, S.; Antony, J.; Ehrlich, S.; Krieg, H. A Consistent and Accurate Ab Initio Parametrization of Density Functional Dispersion Correction (DFT-D) for the 94 Elements H-Pu. *J. Chem. Phys.* **2010**, *132* (15). https://doi.org/10.1063/1.3382344.

(35)   Henkelman, G.; Uberuaga, B. P.; Jónsson, H. Climbing Image Nudged Elastic Band Method for Finding Saddle Points and Minimum Energy Paths. *J. Chem. Phys.* **2000**, *113* (22). https://doi.org/10.1063/1.1329672.

(36)   Henkelman, G.; Jónsson, H. Improved Tangent Estimate in the Nudged Elastic Band Method for Finding Minimum Energy Paths and Saddle Points. *J. Chem. Phys.* **2000**, *113* (22). https://doi.org/10.1063/1.1323224.

(37)   Tang, W.; Sanville, E.; Henkelman, G. A Grid-Based Bader Analysis Algorithm without Lattice Bias. *J. Phys. Condens. Matter* **2009**, *21* (8). https://doi.org/10.1088/0953-8984/21/8/084204.

(38)   Sanville, E.; Kenny, S. D.; Smith, R.; Henkelman, G. Improved Grid-Based Algorithm for Bader Charge Allocation. *J. Comput. Chem.* **2007**, *28* (5). https://doi.org/10.1002/jcc.20575.

(39)   Henkelman, G.; Arnaldsson, A.; Jónsson, H. A Fast and Robust Algorithm for Bader Decomposition of Charge Density. *Comput. Mater. Sci.* **2006**, *36* (3). https://doi.org/10.1016/j.commatsci.2005.04.010.

(40)	Yu, M.; Trinkle, D. R. Accurate and Efficient Algorithm for Bader Charge Integration. *J. Chem. Phys.* **2011**, *134* (6). https://doi.org/10.1063/1.3553716.

(41)	Hjorth Larsen, A.; JØrgen Mortensen, J.; Blomqvist, J.; Castelli, I. E.; Christensen, R.; Dułak, M.; Friis, J.; Groves, M. N.; Hammer, B.; Hargus, C.; Hermes, E. D.; Jennings, P. C.; Bjerre Jensen, P.; Kermode, J.; Kitchin, J. R.; Leonhard Kolsbjerg, E.; Kubal, J.; Kaasbjerg, K.; Lysgaard, S.; Bergmann Maronsson, J.; Maxson, T.; Olsen, T.; Pastewka, L.; Peterson, A.; Rostgaard, C.; SchiØtz, J.; Schütt, O.; Strange, M.; Thygesen, K. S.; Vegge, T.; Vilhelmsen, L.; Walter, M.; Zeng, Z.; Jacobsen, K. W. The Atomic Simulation Environment - A Python Library for Working with Atoms. *J. Phys. Condens. Matter*. 2017. https://doi.org/10.1088/1361-648X/aa680e.

(42)	Bahn, S. R.; Jacobsen, K. W. An Object-Oriented Scripting Interface to a Legacy Electronic Structure Code. *Comput. Sci. Eng.* **2002**, *4* (3). https://doi.org/10.1109/5992.998641.

(43)	Herráez, A. Biomolecules in the Computer: Jmol to the Rescue. *Biochem. Mol. Biol. Educ*. 2006. https://doi.org/10.1002/bmb.2006.494034042644.

(44)	Hanson, R. M. Jmol-a Paradigm Shift in Crystallographic Visualization. *J. Appl. Crystallogr.* **2010**, *43* (5 PART 2). https://doi.org/10.1107/S0021889810030256.

(45)	Herráez, A.; Hanson, R. M.; Glasser, L. *Jmol: An Open-Source Java Viewer for Chemical Structures in 3D*. Angel. *Biochem. Mol. Biol. Educ*.

(46)	Izumi, F.; Momma, K. Three-Dimensional Visualization in Powder Diffraction. In *Solid State Phenom.*; 2007; Vol. 130. https://doi.org/10.4028/www.scientific.net/SSP.130.15.

(47)	Momma, K.; Izumi, F. An Integrated Three-Dimensional Visualization System VESTA Using WxWidgets. *Comm. Crystallogr. Comput. IUCr. News.* **2006**, *7*.

(48)	Momma, K.; Izumi, F. VESTA: A Three-Dimensional Visualization System for Electronic and Structural Analysis. *J. Appl. Crystallogr.* **2008**, *41* (3). https://doi.org/10.1107/S0021889808012016.

(49)	Momma, K.; Izumi, F. VESTA 3 for Three-Dimensional Visualization of Crystal, Volumetric and Morphology Data. *J. Appl. Crystallogr.* **2011**, *44* (6). https://doi.org/10.1107/S0021889811038970.

(50)	Chen, W. J.; Zhai, H. J.; Zhang, Y. F.; Huang, X.; Wang, L. S. On the Electronic and Structural Properties of Tri-Niobium Oxide Clusters Nb3On- (n = 3-8): Photoelectron Spectroscopy and Density Functional Calculations. *J. Phys. Chem. A* **2010**, *114* (19). https://doi.org/10.1021/jp102439v.

(51)	Ganguly, S.; Kabir, M.; Autieri, C.; Sanyal, B. Manipulating Magnetism of MnO Nano-Clusters by Tuning the Stoichiometry and Charge State. *J. Phys. Condens. Matter* **2015**, *27* (5). https://doi.org/10.1088/0953-8984/27/5/056002.

(52)	Li, S.; Dixon, D. A. Molecular Structures and Energetics of the (ZrO2)n and (HfO2)n (n = 1-4) Clusters and Their Anions. *J. Phys. Chem. A* **2010**, *114* (7). https://doi.org/10.1021/jp910310j.

(53) Hamad, S.; Catlow, C. R. A.; Woodley, S. M.; Lago, S.; Mejías, J. A. Structure and Stability of Small TiO2 Nanoparticles. *J. Phys. Chem. B* **2005**, *109* (33). https://doi.org/10.1021/jp0521914.

(54) Nagase, S.; Morokuma, K. An Ab Initio Molecular Orbital Study of Organic Reactions. The Energy, Charge, and Spin Decomposition Analyses at the Transition State and along the Reaction Pathway. *J. Am. Chem. Soc.* **1978**, *100* (6). https://doi.org/10.1021/ja00474a005.

(55) Kitaura, K.; Morokuma, K. A New Energy Decomposition Scheme for Molecular Interactions within the Hartree-Fock Approximation. *Int. J. Quantum. Chem.* **1976**, *10* (2). https://doi.org/10.1002/qua.560100211.

(56) Diefenbach, A.; Bickelhaupt, F. M. Activation of H-H, C-H, C-C, and C-Cl Bonds by Pd(0). Insight from the Activation Strain Model. *J. Phys. Chem. A* **2004**, *108* (40). https://doi.org/10.1021/jp047986.

(57) Diefenbach, A.; de Jong, G. T.; Bickelhaupt, F. M. Fragment-Oriented Design of Catalysts Based on the Activation Strain Model§. *Mol. Phys.* **2005**, *103* (6–8). https://doi.org/10.1080/00268970412331333546.

(58) Bickelhaupt, F. M.; Houk, K. N. Analyzing Reaction Rates with the Distortion/Interaction-Activation Strain Model. *Angew. Chem. – Int. Ed*. 2017. https://doi.org/10.1002/anie.201701486.

(59) Ess, D. H.; Houk, K. N. Distortion/Interaction Energy Control of 1,3-Dipolar Cycloaddition Reactivity. *J. Am. Chem. Soc.* **2007**, *129* (35). https://doi.org/10.1021/ja0734086.

(60) Ess, D. H.; Houk, K. N. Theory of 1,3-Dipolar Cycloadditions: Distortion/Interaction and Frontier Molecular Orbital Models. *J. Am. Chem. Soc.* **2008**, *130* (31). https://doi.org/10.1021/ja800009z.

(61) Bader, R. F. W. A Quantum Theory of Molecular Structure and Its Applications. *Chem. Rev.* **1991**, *91* (5). https://doi.org/10.1021/cr00005a013.

(62) Otero-de-la-Roza, A.; Blanco, M. A.; Pendás, A. M.; Luaña, V. Critic: A New Program for the Topological Analysis of Solid-State Electron Densities. *Comput. Phys. Commun.* **2009**, *180* (1). https://doi.org/10.1016/j.cpc.2008.07.018.

(63) Otero-De-La-Roza, A.; Johnson, E. R.; Luaña, V. Critic2: A Program for Real-Space Analysis of Quantum Chemical Interactions in Solids. *Comput. Phys. Commun.* **2014**, *185* (3). https://doi.org/10.1016/j.cpc.2013.10.026.

(64) Wang, J.; Ma, Y.; Mahapatra, M.; Kang, J.; Senanayake, S. D.; Tong, X.; Stacchiola, D. J.; White, M. G. Surface Structure of Mass-Selected Niobium Oxide Nanoclusters on Au(111). *Nanotechnology* **2021**, *32* (47). https://doi.org/10.1088/1361-6528/ac1cc0.

Supporting Information: Mechanism of Stoichiometrically Governed Titanium Oxide Brownian Tree Formation on Stepped Au(111)

Robert H. Lavroff [†], Jason Wang[º], Michael G. White[º][‖], Philippe Sautet[*][†][·][‡], and Anastassia N. Alexandrova[*][†][‡]

[†]Department of Chemistry and Biochemistry, University of California, Los Angeles, Los Angeles, California 90095, United States

[·]Department of Chemical Engineering, University of California, Los Angeles, Los Angeles, California 90095, United States

[‡]California NanoSystems Institute, Los Angeles, California 90095, United States

[º]Department of Chemistry, Stony Brook University, Stony Brook, New York 11794, USA

[‖]Chemistry Division, Brookhaven National Laboratory, Upton, New York 11973, USA

[*]Corresponding authors' emails: sautet@ucla.edu, ana@chem.ucla.edu
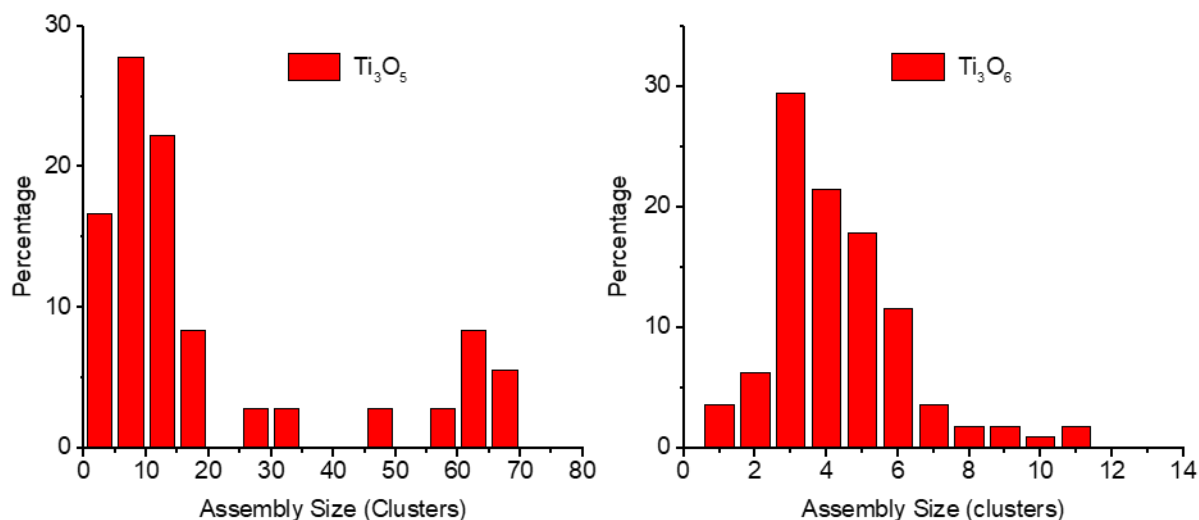
Figure S1: Size distributions of the cluster assemblies as determined from STM images of the as-deposited surfaces at room temperature: (left) Ti_3O_5/Au(111) and (right) Ti_3O_6/Au(111). The cluster size distributions above were obtained from the distributions of cluster assembly sizes (areas in nm^2) extracted from STM images of the Ti_3O_5/Au(111) and Ti_3O_6/Au(111) surfaces (WSxM image software) and dividing them by the size (area) of a single Ti_3O_5 or Ti_3O_6 cluster. The latter were estimated from STM images on surfaces with relatively low cluster coverage where it was possible image isolated monomers, dimers, etc. See reference[1] for large and small scale images of the Ti_3O_5/Au(111) and Ti_3O_6/Au(111) surfaces.

Note S1: Discussion of BLDA and sampling strategy: Initial structures for global optimization should be created to be less prone to a Self-Consistent Field (SCF) convergence problem. Also, by generating initial structures wisely, the computational cost to search in a chemically unfavorable configuration space can be significantly reduced. One may do this by restricting the distance of atoms to their closest and second closest neighbor atoms to follow a Gaussian distribution. This generation algorithm is called Bond Length Distribution Algorithm (BLDA).[2,3] PGOPT global optimization codes are available open-source at the following GitHub repository: https://github.com/hczhai/PGOPT

Following use of BLDA to obtain optimized titanium oxide monomer structures in the gas phase, these clusters were landed on the Au surface in all possible geometries, accounting for symmetry. The GM clusters in the gas phase were generally triangular Ti clusters with O atoms arranged such that a single in-plane reflection axis was present, i.e. the symmetry of an isosceles triangle. Thus, for such a structure, geometry optimizations were performed landing the cluster at two of its points (the third being symmetrically redundant), two of its edges (the third being symmetrically redundant), and flat on both of its sides. For clusters of lower symmetry, all points, edges, and sides were considered. For sampling on the stepped Au surface, additional geometries were considered due to the increased degrees of freedom brought on by thr step edge. For example, a triangular cluster landed upon the terrace on its point could either be parallel or perpendicular to the step edge. Possible considerations were considered and optimized *ad nauseum* at the step edge, and the presence of many redundant structures upon geometry optimization strongly indicates sufficient sampling.

Note S2: Calculation of binding and dimerization energies: Biding energies for clusters on Au surfaces were calculated by subtracting the DFT energy of the separate cluster (in the gas phase) and slab from that of the bound cluster, i.e.:

$$E_{binding} = E_{full\ system} - E_{cluster} - E_{slab}$$

Dimerization energies were calculated by subtracting twice the DFT binding energy of the monomer from the DFT binding energy of the dimer, i.e.

$$E_{dimerization} = E_{dimer\ binding} - 2E_{monomer\ binding}$$

Note S3: Benchmarking DFT accuracy: To assure accurate DFT energies, a brief test was conducted in which the adsorption energy for atomic O on Au(111) was calculated with the settings used in this study and compared to past experimental and DFT literature. This calculated energy was 2.80 eV, in excellent agreement with DFT literature (2.77 eV)[4] and good agreement with experiment (2.54 eV).[5]

Top 5 lowest-energy isomers in gas phase

Structures in this SI are visualized using the graphical user interface from the Atomic Simulation Environment (ASE).[6,7]
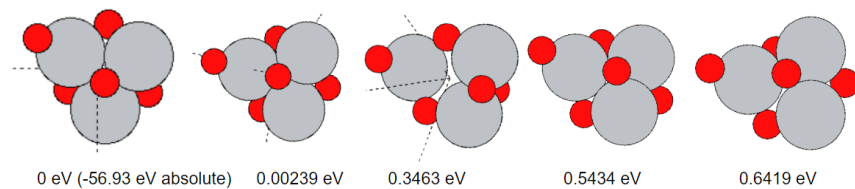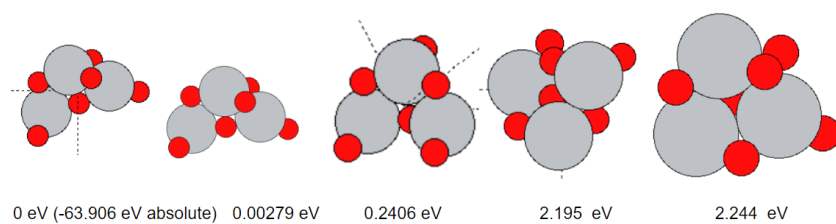

| 0 eV (-56.93 eV absolute) | 0.00239 eV | 0.3463 eV | 0.5434 eV | 0.6419 eV |

Figure S2: Ti3O5 gas phase minima

| 0 eV (-63.906 eV absolute) | 0.00279 eV | 0.2406 eV | 2.195 eV | 2.244 eV |

Figure S3: Ti3O6 gas phase minima
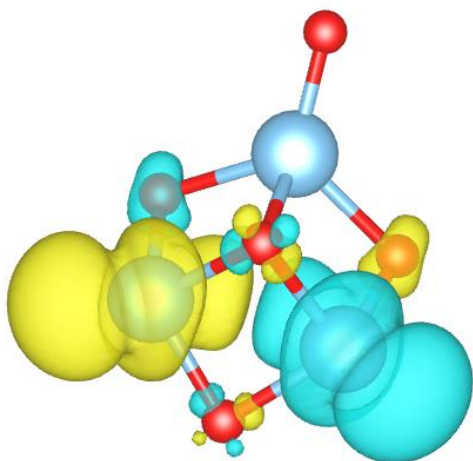
Figure S4: Spin density of Ti3O5 gas-phase GM cluster

Full CINEB plots
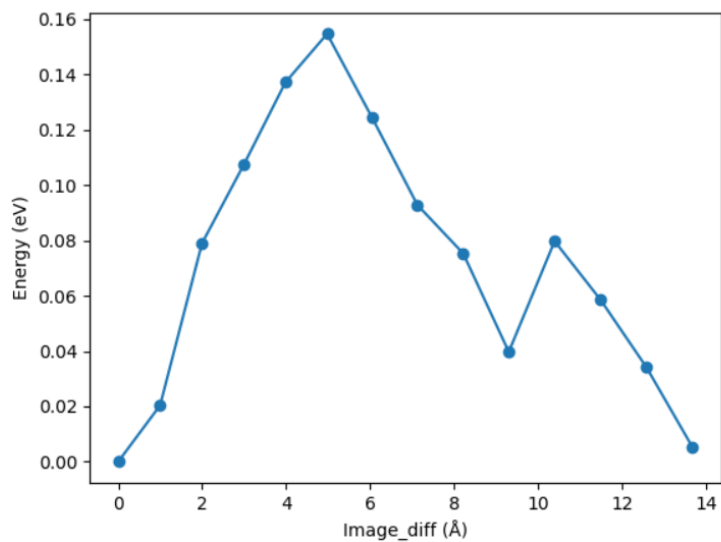
Figure S5: Translation of LM1 from one minimum energy site on the unit cell to another.
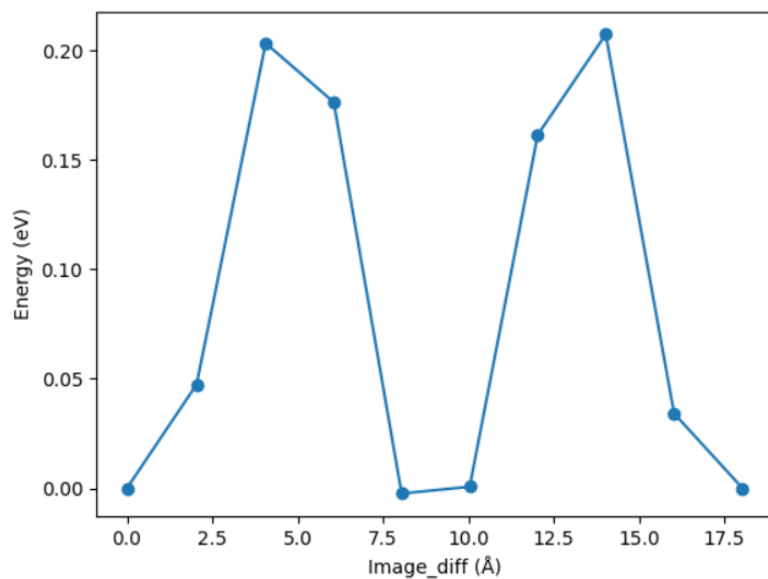
Figure S6: Translation of GM across a lattice direction. The two near-identical peaks represent translation over two separate Au atoms along the lattice vector.
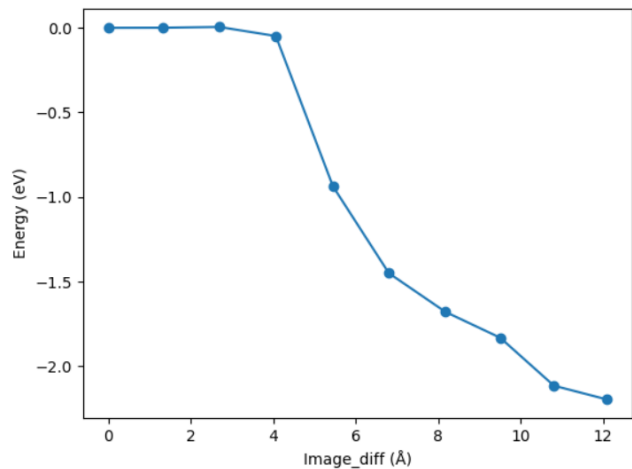
Figure S7: Dimerization of two GM Ti3O5 monomers, shown to be barrierless.
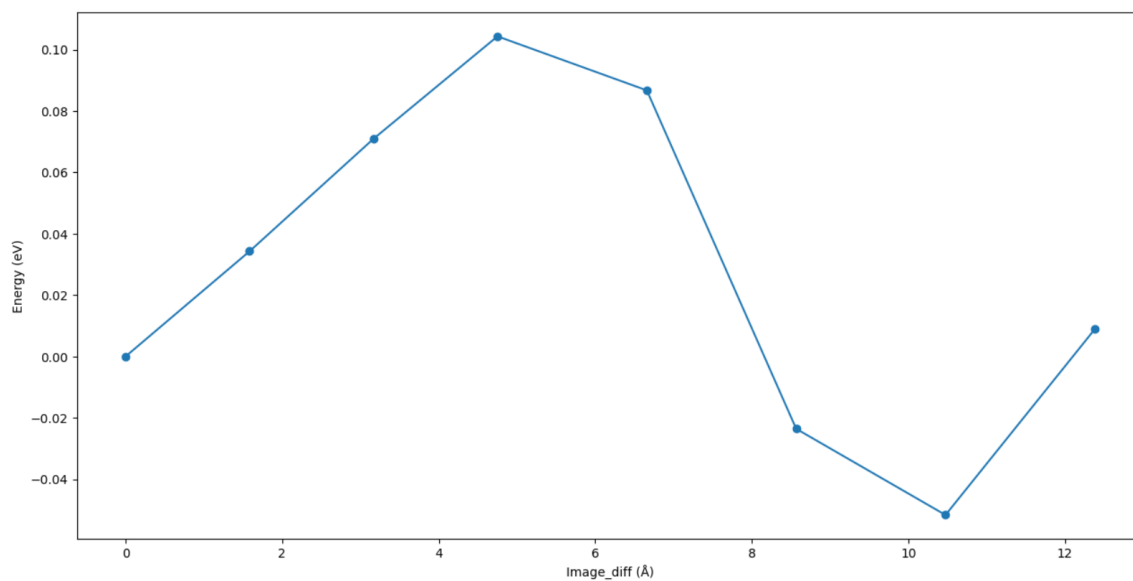

Figure S8: Diffusion barrier of the Ti3O6 terrace GM along one Au atom of the 111 terrace lattice vector.
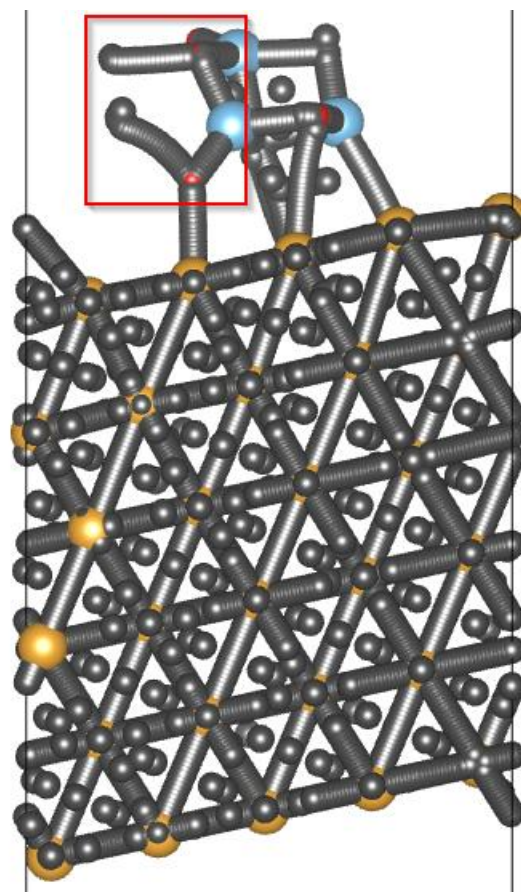
Figure S9: QTAIM bond critical points (BCPs) of the 111 terrace Ti_3O_6 GM placed on a step supercell. The BCPs boxed in red show interaction of the cluster with the step, and this structure relaxes to the 553 step GM. This QTAIM analysis was performed with the critic2 software, discarding spurious BCPs with less than 5E-04 a.u. of electron density.[8,9]
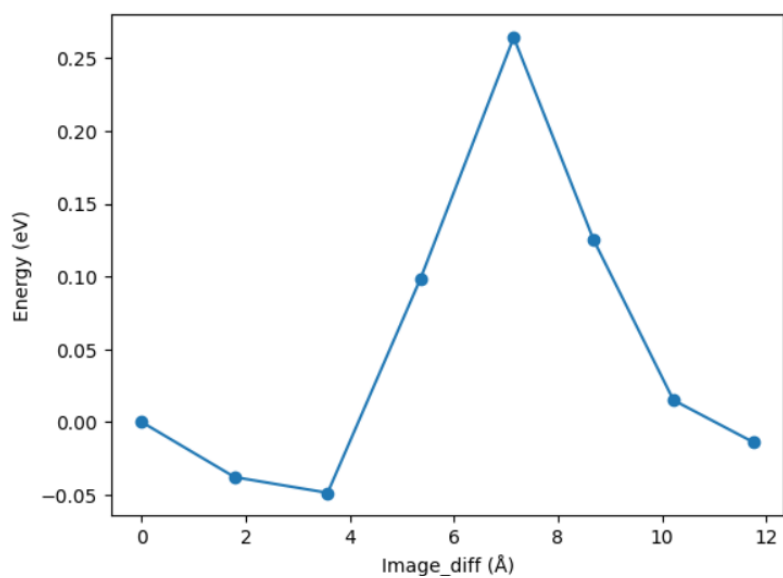

Figure S10: Diffusion barrier of the Ti3O6 step GM structure along one Au atom of the 553 step.
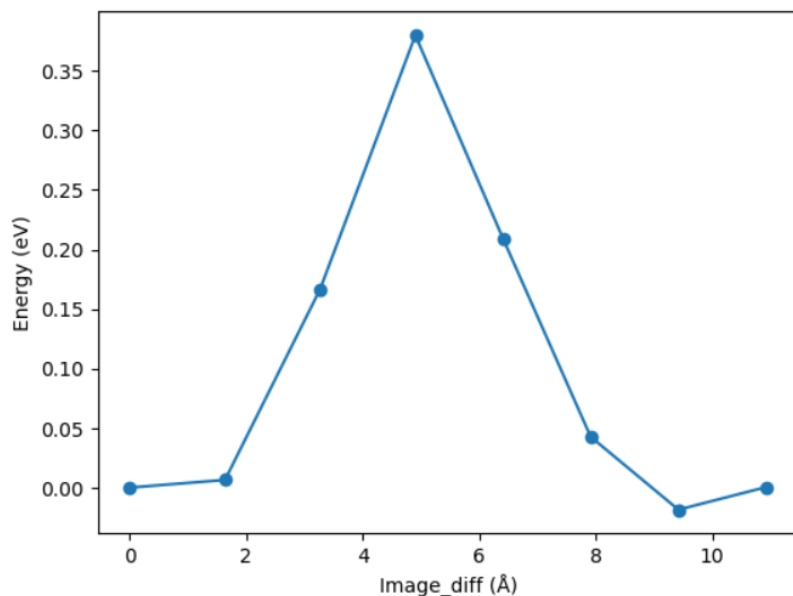
Figure S11: Diffusion barrier of the Ti3O6 step LM1 structure along one Au atom of the 553 step.

Note S4: STM simulations: Simulations of STM images from VASP partial charge density (PARCHG) files were carried out with the STM_2DScan script of Shuang Lueng, available here: https://github.com/ShuangLeung/STM_2DScan. Benchmarking was carried out in constant current mode and constant height mode (heights from 3 to 9 angstroms from the topmost atom in the unit cell) at bias potentials from +2.0 eV to -2.0 eV in increments of 0.1 eV. The image in the main text Figure 7 was selected for its clarity of Au, Ti, and O atoms along the dendritic wire's supercell.

(1)   Goodman, K. R.; Wang, J.; Ma, Y.; Tong, X.; Stacchiola, D. J.; White, M. G. Morphology and Reactivity of Size-Selected Titanium Oxide Nanoclusters on Au(111). *J. Chem.l Phys.* **2020**, *152* (5). https://doi.org/10.1063/1.5134453.

(2)   Zandkarimi, B.; Alexandrova, A. N. Dynamics of Subnanometer Pt Clusters Can Break the Scaling Relationships in Catalysis. *J. Phys. Chem. Lett* **2019**, *10* (3). https://doi.org/10.1021/acs.jpclett.8b03680.

(3)   Zhai, H.; Alexandrova, A. N. Ensemble-Average Representation of Pt Clusters in Conditions of Catalysis Accessed through GPU Accelerated Deep Neural Network Fitting Global Optimization. *J. Chem. Theory. Comput.* **2016**, *12* (12). https://doi.org/10.1021/acs.jctc.6b00994.

(4)   Santiago-Rodríguez, Y.; Herron, J. A.; Curet-Arana, M. C.; Mavrikakis, M. Atomic and Molecular Adsorption on Au(111). *Surf. Sci.* **2014**, *627*. https://doi.org/10.1016/j.susc.2014.04.012.

(5)   Xu, Y.; Mavrikakis, M. Adsorption and Dissociation of O2 on Gold Surfaces: Effect of Steps and Strain. *J. Phys. Chem. B* **2003**, *107* (35). https://doi.org/10.1021/jp034380x.

(6)   Hjorth Larsen, A.; JØrgen Mortensen, J.; Blomqvist, J.; Castelli, I. E.; Christensen, R.; Dułak, M.; Friis, J.; Groves, M. N.; Hammer, B.; Hargus, C.; Hermes, E. D.; Jennings, P. C.; Bjerre Jensen, P.;

Kermode, J.; Kitchin, J. R.; Leonhard Kolsbjerg, E.; Kubal, J.; Kaasbjerg, K.; Lysgaard, S.; Bergmann Maronsson, J.; Maxson, T.; Olsen, T.; Pastewka, L.; Peterson, A.; Rostgaard, C.; SchiØtz, J.; Schütt, O.; Strange, M.; Thygesen, K. S.; Vegge, T.; Vilhelmsen, L.; Walter, M.; Zeng, Z.; Jacobsen, K. W. The Atomic Simulation Environment - A Python Library for Working with Atoms. *J. Phys. Condens. Matter*. 2017. https://doi.org/10.1088/1361-648X/aa680e.

(7)   Bahn, S. R.; Jacobsen, K. W. An Object-Oriented Scripting Interface to a Legacy Electronic Structure Code. *Comput. Sci. Eng.* **2002**, *4* (3). https://doi.org/10.1109/5992.998641.

(8)   Otero-de-la-Roza, A.; Blanco, M. A.; Pendás, A. M.; Luaña, V. Critic: A New Program for the Topological Analysis of Solid-State Electron Densities. *Comput. Phys. Commun.* **2009**, *180* (1). https://doi.org/10.1016/j.cpc.2008.07.018.

(9)   Otero-De-La-Roza, A.; Johnson, E. R.; Luaña, V. Critic2: A Program for Real-Space Analysis of Quantum Chemical Interactions in Solids. *Comput. Phys. Commun.* **2014**, *185* (3). https://doi.org/10.1016/j.cpc.2013.10.026.